Progress In Electromagnetics Research B, Vol. 48, 99–113, 2013

MICROWAVE DOPPLER SPECTRA OF SEA ECHOES AT HIGH INCIDENCE ANGLES: INFLUENCES OF LARGE-SCALE WAVES

Yunhua Wang[1, *], Yanmin Zhang[2], and Lixin Guo[3]

[1]Ocean Remote Sensing Institute, Ocean University of China, Qingdao 266003, China

[2]College of Information Science & Engineering, Ocean University of China, Qingdao 266100, China

[3]School of Science, Xidian University, Xi'an 710071, China

Abstract—Within the framework of the composite surface scattering model, analytical formulas for Doppler shift and bandwidth of radar echoes backscattered from time-varying sea surface are derived in the forms of three-dimensional integrals. In our derivations, the influences of the tilt modulation (TM), the hydrodynamic modulation (HM), the shadow and the curvature of large-scale undulating waves are all taken into account for achieving more reasonable results. Comparisons between our theoretical curves and the results obtained directly by exact numerical method demonstrate that our formulas can improve the simulated results. On the other hand, the simulations by our formulas can also help to estimate the effects of the TM, the HM, and the shadow of large-scale waves on Doppler behaviors individually. We find that the predicted Doppler shifts are always larger in HH-polarization than in VV-polarization due to the TM. Meanwhile, the simulations also show that the predicted Doppler shifts for both HH- and VV-polarizations would become larger when the HM is considered. In addition, at low-grazing angles (LGA), the shadow effect results in a rapid increase in the predicted Doppler shift, and on the contrary makes the bandwidth narrower.

Received 30 December 2012, Accepted 21 January 2013, Scheduled 24 January 2013

* Corresponding author: Yunhua Wang (yunhuawang@ouc.edu.cn).

1. INTRODUCTION

Doppler spectrum of microwave signal backscattered from oceanic surface reflects the distribution of the power-weighted line-of-sight velocity of the scattering facets and carries more information on the sea state than does the radar cross section (RCS). Thus, the study on Doppler spectrum is of practical importance in a number of research areas such as sea surface wind retrieving, sea waves monitoring and oceanic surface current measuring. In recent years, the properties of microwave Doppler spectrum from sea surface have been the subject of extensive investigations, both experimentally and theoretically [1–17]. Over 40 years ago, experiment results showed a significant difference between the co-polarized Doppler shifts at moderate to high incidence angles, with the Doppler shifts of horizontally polarized (HH-polarization) signals being larger than the results corresponding to vertically polarized (VV-polarization) signals [18, 19]. To explain this anomalous property, investigators have been postulated that this difference between the co-polarized Doppler shifts is induced by scattering from "fast scatterers" which are more prominent in HH polarized signal than in VV [20, 21]. And the so-called "fast scatterers" are always considered as the "bound waves" which localize on the front faces of large scale waves in the vicinity of their crests and propagate with a velocity close to the phase velocity of the corresponding large scale gravity waves. However, the recent investigations on Doppler spectra utilizing asymptotic electromagnetic wave scattering theories [14–17] and exact numerical methods [9, 10], in which the influence of the scattering fields from "fast scatterers" is not considered, have also shown significant differences between co-polarized predicated Doppler shifts. Therefore, the works in [9, 10, 14–17] imply that not only the so-called "fast scatterers" but also the other mechanisms may be required to explain the observed Doppler spectra at moderate- and low-grazing incidence angles. Since Doppler spectra are weighted by received power, some scattering mechanisms, such as the TM, the HM, the shadow and the curvature of large-scale waves, may be responsible for the Doppler shift and the bandwidth of microwave scattering from oceanic surface. In [22], a Doppler spectrum model was proposed by Romeiser and Thompson using a composite surface scattering approach. In their model, the effects of the TM and the HM are taken into account. However, it should be noted that the effects from the shadow and the curvature of large-scale waves are not discussed in [22], and thus Romeiser's model is invalid at LGA. In a previous paper [17], the authors developed a semi-numerical method to investigate the microwave Doppler properties from time-varying sea

surface within the framework of composite surface scattering model. The simulations in [17] show that the TM, the HM, and the shadow of large-scale undulating waves make a notable influence on Doppler shift. Meanwhile, the shadow also makes the bandwidth falling off at LGA.

In this paper, an analytical model for microwave Doppler of sea echoes at high incidence angles when the TM, the HM, the shadow and the curvature of large-scale undulating waves are all taken into consideration, is presented. In Section 2, a linear hydrodynamic theory is employed to simulate the composite sea surface. Meanwhile, we suppose that the 1D short ocean gravity waves can be described by a Pierson-Moskowitz (P-M) spectrum [9, 10] with a $|K|^{-3}$ dependence, and then the hydrodynamic modulation function (HMF) of short gravity ripples by large-scale waves is derived utilizing the weak hydrodynamic interaction theory [23, 24]. In Sections 3–4, the analytical formulas for Doppler shift and bandwidth are derived when the effects of large-scale waves shadow and curvature are also taken into account. The Section 5 is devoted to the results and the comments, while the concluding remarks and perspectives are provided in Section 6.

2. THE COMPOSITE SURFACE MODEL

Within the framework of the composite surface scattering model, the total sea surface is partitioned into small-scale and large-scale waves, such that

$$Z(x,t) = Z_s(x,t) + Z_l(x,t) \tag{1}$$

where $Z_l(x,t)$ represents the large-scale portion of the surface elevation. $Z_s(x,t)$, which has been modulated by large-scale waves, denotes small-scale roughness with $2k_i \cos\theta_i Z_s(x,t) \ll 1.0$. k_i is the wave number of microwave and θ_i is the incidence angle. If we assume that $Z_l(x,t)$ and $Z_s(x,t)$ are statistically independent, the full wave-height spectrum, i.e., $W(K)$, can be written as

$$W(K) = W_{ms}(K) + W_l(K) \tag{2}$$

where $W_{ms}(K)$, for $(K > K_C)$, is the wave-height spectrum of small-scale surface roughness, and $W_l(K) = W(K)$, for $(K \leq K_C)$, is a low-frequency part that forms the large-scale surface roughness. The cutoff wave number K_C can range from $K_{\text{Bragg}}/6$ to $K_{\text{Bragg}}/3$ [28], here we choose the former value. $K_{\text{Bragg}}(\theta_i) = 2k_i \sin\theta_i$ is the Bragg wave number.

Using the linear hydrodynamic theory, the irregular sea surface can be described as a superposition of harmonics with different random

amplitudes and random phases. Based on the hydrodynamic model given in [9, 10], the stochastic large-scale waves can be simulated by

$$Z_l(x,t) = \frac{1}{L}\sum_n \xi(K_n,t)\exp(jK_nx) \tag{3}$$

In (3), $j=\sqrt{-1}$, L is the length of the sea surface, $\xi(K_n,t)$ denotes the spatial Fourier component of the linear surface at any time t as

$$\begin{aligned}\xi(K_n,t) \;=\; & \frac{2\pi}{\sqrt{2\Delta K}}\Big\{\gamma_n\sqrt{W_l(K_n)}\exp(-j\omega_n t) \\ & +\gamma^*_{-n}\sqrt{W_l(-K_n)}\exp[j\omega_n t]\Big\}\end{aligned} \tag{4}$$

γ_n is the complex random number with a Gaussian probability density function and unit variance, the rotational frequency $\omega_n = \sqrt{g|K_n|}$, and g is the gravity acceleration constant. $W_l(K)$ represents the 1D Pierson-Moskowitz spectrum [9, 10], i.e.,

$$W_l(K) = W_{\text{P-M}}(K) = \frac{0.0081}{4K^3}\exp\left\{-\frac{0.74g^2}{K^2U^4_{19.5}}\right\} \tag{5}$$

where $U_{19.5}$ is the wind speed at a height of 19.5 m above sea surface.

In the same way, based on the linear hydrodynamic theory, we can also obtain that

$$S_l(x,t) \;=\; \frac{1}{L}\sum_n jK_n\xi(K_n,t)\exp(jK_nx) \tag{6}$$

$$D_l(x,t) \;=\; -\frac{1}{L}\sum_n K_n^2\xi(K_n,t)\exp(jK_nx) \tag{7}$$

$$V_{xl}(x,t) \;=\; \frac{1}{L}\sum_n \omega_n\xi(K_n,t)\exp(jK_nx) \tag{8}$$

$$V_{zl}(x,t) \;=\; -\frac{1}{L}\sum_n j\omega_n\xi(K_n,t)\exp(jK_nx) \tag{9}$$

and

$$H_y(x,t) = \frac{1}{L}\sum_n R^{hydr}(K_n)\xi(K_n,t)\exp(jK_nx) \tag{10}$$

where $S_l(x,t)$ and $D_l(x,t)$ represent the surface slope and the second-order derivative of the large-scale waves with respect to x. $V_{xl}(x,t)$ and $V_{zl}(x,t)$ denote the horizontal- and the vertical-components of large-scale waves' orbital velocity. H_y is the spectral disturbance induced by the HM. $R^{hydr} = 3.5|K|\omega(\omega - j\mu)/(\omega^2+\mu^2)$ is the HMF for 1-D waves [16, 17], μ denotes the relaxation rate and has to be determined

by experiment. Because the value of μ is poorly known so far, here we take $\mu = 0\,\mathrm{s}^{-1}$, and then R^{hydr} reduces to that of Longuet-Higgins [10] which makes the short waves converge at the crests and spread out at troughs of long waves. Thus, the roughness spectrum for the short ripples modulated by large-scale waves can be written as [16, 17]

$$W_{ms}(K_s) = W_s(K_s)(1.0 + H_y) \tag{11}$$

where W_s denotes the spectrum which is not modulated by large-scale waves.

3. THE JOINT PROBABILITY DENSITY FUNCTION

Let $P_6(Z_l, S_l, D_l, V_{xl}, V_{zl}, H_y)$ denotes the joint probability density function (PDF) of vector $[Z_l, S_l, D_l, V_{xl}, V_{zl}, H_y]$. Because Z_l, S_l, D_l, V_{xl}, V_{zl} and H_y are all stochastic processes obeying Gaussian distribution, then the six-dimensional PDF $P_6(Z_l, S_l, D_l, V_{xl}, V_{zl}, H_y)$ can be written as [25]

$$P_6(Z_l, S_l, D_l, V_{xl}, V_{zl}, H_y) = \frac{1}{(2\pi)^3\sqrt{|\mathbf{M}|}} \exp\left[-\frac{1}{2}\mathbf{X}^T\mathbf{M}^{-1}\mathbf{X}\right] \tag{12}$$

In (12), the vector $\mathbf{X}^T = [Z_l, S_l, D_l, V_{xl}, V_{zl}, H_y]$, $\mathbf{M}$ is the corresponding covariance matrix of $\mathbf{X}$

$$\mathbf{M} = \begin{bmatrix} \sigma^2_{Z_l} & 0 & \sigma^2_{Z_lD_l} & \sigma^2_{Z_lV_{xl}} & 0 & \sigma^2_{Z_lH_y} \\ 0 & \sigma^2_{S_l} & 0 & 0 & \sigma^2_{S_lV_{zl}} & 0 \\ \sigma^2_{Z_lD_l} & 0 & \sigma^2_{D_l} & \sigma^2_{D_lV_{xl}} & 0 & \sigma^2_{D_lH_y} \\ \sigma^2_{Z_lV_{xl}} & 0 & \sigma^2_{D_lV_{xl}} & \sigma^2_{V_{xl}} & 0 & \sigma^2_{H_yV_{xl}} \\ 0 & \sigma^2_{S_lV_{zl}} & 0 & 0 & \sigma^2_{V_{zl}} & 0 \\ \sigma^2_{Z_lH_y} & 0 & \sigma^2_{D_lH_y} & \sigma^2_{H_yV_{xl}} & 0 & \sigma^2_{H_y} \end{bmatrix} \tag{13}$$

In (12), $|\mathbf{M}|$ denotes the determinant of the covariance matrix.

4. DOPPLER SHIFT AND BANDWIDTH

Doppler shift f_{Dpp} and bandwidth δf_{pq} are generally considered as the first- and the second-order moments of Doppler spectrum and weighted by scattering power [22, 26]. If the effect of Bragg frequency is removed, then, the Doppler shift f'_{Dpp} and the bandwidth δf_{pq} can be defined as

$$f'_{Dpp} = \frac{\langle f\sigma'_{pq}\rangle}{\langle\sigma'_{pq}\rangle} \tag{14}$$

and

$$\delta f_{pp}^2 = \frac{\left\langle f^2 \sigma'_{pq} \right\rangle}{\left\langle \sigma'_{pq} \right\rangle} - \left[f'_{Dpp} \right]^2 \tag{15}$$

where $\langle \bullet \rangle$ denotes ensemble average, $\sigma'_{pq} = \sigma^0_{pp} \left[1 + H_y\right] \cdot C_{pp} \cdot Sh$, and Doppler frequency $f = \frac{k_i}{\pi} \left(V_{zl} \cos\theta_i + V_{xl} \sin\theta_i\right)$.

Converting Equations (14) and (15) into integral forms, we can obtain that

$$f'_{Dpp} = \frac{\int\limits_{-\infty}^{\infty} f \sigma^0_{pp}\left(\theta'_i\right) \left[1 + H_y\right] C_{pp}\, Sh \cdot P_6\, dZ_l dS_l dD_l dV_{zl} dV_{xl} dH_y}{\sigma_{pp}} \tag{16}$$

and

$$\delta f_{pp}^2 = \frac{\int\limits_{-\infty}^{\infty} f^2 \sigma^0_{pp}\left(\theta'_i\right) \left[1 + H_y\right] C_{pp}}{Sh \cdot P_6 dZ_l dS_l dD_l dV_{zl} dV_{xl} dH_y} - \left[f'_{Dpp} \right]^2 \tag{17}$$

In (16) and (17), $\sigma^0_{pp}(\theta'_i)$ denotes the first-order backscattering coefficient from the small-scale waves for the pp (HH or VV) polarization [27], C_{pp} and Sh denote the modified factor of curvature proposed by Voronovich and Zavorotny in [28] and the shadow function proposed by Smith in [29], respectively.

Substituting (12) into (16) and (17) and performing integration on V_{zl}, V_{xl}, and H_y, we can obtain that

$$\begin{aligned}
& f'_{Dpp(H_y+Vx+tilt+shadow+cur)} \\
= & -\frac{4\pi \left|\mathbf{M}\right|}{\lambda \sigma_{pp} \sqrt{B_{44} B_{55}}} \sqrt{\frac{\pi}{\mu}} \iint \int \sigma^0_{pp}\left(\theta'_i\right) \Psi \cdot C_{pp} \cdot Sh \cdot \exp\left(\frac{d^2}{\mu}\right) \\
& \cdot \exp\left[\frac{(B_{52} S_l)^2}{2\left|\mathbf{M}\right| B_{55}} + \frac{(B_{14} Z_l + B_{34} D_l)^2}{2\left|\mathbf{M}\right| B_{44}}\right] \left\{ \cos\theta_i \frac{B_{52} S_l}{B_{55}} \right. \\
& + \sin\theta \frac{(B_{14} Z_l + B_{34} D_l)}{B_{44}} + \sin\theta \frac{B_{64}}{B_{44}} \frac{1}{2\mu} \left(1 + 2\frac{d^2}{\mu}\right) + \left[\sin\theta \frac{B_{64}}{B_{44}} \right. \\
& \left. \left. + \cos\theta_i \frac{B_{52} S_l}{B_{55}} + \sin\theta \frac{(B_{14} Z_l + B_{34} D_l)}{B_{44}} \right] \frac{d}{\mu} \right\} dZ_l dS_l dD_l
\end{aligned} \tag{18}$$

$$\begin{aligned}
& \delta f^2_{pp(H_y+Vx+tilt+shadow+cur)} \\
= & \frac{8\pi \left|\mathbf{M}\right|}{\lambda^2 \sigma_{pp} \sqrt{B_{44} B_{55}}} \iiint \sigma^0_{pp}\left(\theta'_i\right) \Psi \cdot C_{pp} \cdot Sh \cdot \exp\left[\frac{(B_{52} S_l)^2}{2\left|\mathbf{M}\right| B_{55}}\right] \\
& \cdot \exp\left(\frac{(B_{14} Z_l + B_{34} D_l)^2}{2\left|\mathbf{M}\right| B_{44}}\right) \left\{ \alpha \exp\left(\frac{d^2}{\mu}\right) \sqrt{\frac{\pi}{\mu}} \right.
\end{aligned}$$

$$+\beta\frac{d}{\mu}\sqrt{\frac{\pi}{\mu}}\exp\left(\frac{d^2}{\mu}\right)+(\gamma+\chi)\frac{1}{2\mu}\sqrt{\frac{\pi}{\mu}}\left(1+2\frac{d^2}{\mu}\right)\exp\left(\frac{d^2}{\mu}\right)$$
$$+\chi\frac{d}{2\mu^2}\left(3+\frac{2d^2}{\mu}\right)\sqrt{\frac{\pi}{\mu}}\exp\left(\frac{d^2}{\mu}\right)\Bigg\}dZ_l dS_l dD_l-\left[f'_{Dpp}\right]^2 \quad (19)$$

where $\mu=\frac{B_{66}B_{44}-B_{64}^2}{2|\mathbf{M}|B_{44}}$, $d=\frac{(B_{14}Z_l+B_{34}D_l)B_{64}-(B_{16}Z_l+B_{36}D_l)B_{44}}{2|\mathbf{M}|B_{44}}$, $\alpha=\sin^2\theta_i\frac{|\mathbf{M}|}{B_{44}}+\cos^2\theta_i\frac{|\mathbf{M}|}{B_{55}}(1+\frac{(B_{52}S_l)^2}{|\mathbf{M}|B_{55}})+2\cos\theta_i\sin\theta_i\frac{B_{52}S_l(B_{14}Z_l+B_{34}D_l)}{B_{55}B_{44}}+\sin^2\theta_i\frac{(B_{14}Z_l+B_{34}D_l)^2}{B_{44}^2}$, $\beta=\cos^2\theta_i\frac{|\mathbf{M}|}{B_{55}}(1+\frac{(B_{52}S_l)^2}{|\mathbf{M}|B_{55}})+2\cos\theta_i\sin\theta_i\frac{B_{52}S_l(B_{14}Z_l+B_{34}D_l)+B_{52}S_lB_{64}}{B_{55}B_{44}}+\sin^2\theta_i\frac{|\mathbf{M}|}{B_{44}}+\sin^2\theta_i\frac{2(B_{14}Z_l+B_{34}D_l)B_{64}}{B_{44}^2}+\sin^2\theta_i\frac{(B_{14}Z_l+B_{34}D_l)^2}{B_{44}^2}$, $\gamma=2A_{64}\sin^2\theta_i\frac{(B_{14}Z_l+B_{34}D_l)}{A_{44}^2}+2\cos\theta_i\sin\theta_i\frac{B_{52}B_{64}}{B_{55}B_{44}}S_l$, $\chi=\sin^2\theta_i\frac{B_{64}^2}{B_{44}^2}$, $\Psi=\frac{1}{8\pi^3\sqrt{|\mathbf{M}|}}\exp\left\{-\frac{B_{11}Z_l^2+2B_{31}D_lZ_l+B_{22}S_l^2+B_{33}D_l^2}{2|\mathbf{M}|}\right\}$, $\theta'_i=\arccos[(S_l\sin\theta_i+\cos\theta_i)/(S_l^2+1)]$, B_{ij} denotes the cofactor of the element m_{ij} of $|\mathbf{M}|$.

If we neglect the effect of the HM in (16) and (17), (18) and (19) can be simplified as

$$f'_{Dpp(Vx+tilt+shadow+Cur)}$$
$$=-\frac{4\pi|\mathbf{M}|}{\lambda\sigma_{pp}\sqrt{B_{44}B_{55}}}\sqrt{\frac{\pi}{\mu}}\iint\int\sigma^0_{pp}(\theta'_i)\,\Psi\cdot C_{pp}\cdot Sh$$
$$\cdot\exp\left\{\frac{d^2}{\mu}+\frac{(B_{52}S_l)^2}{2|\mathbf{M}|B_{55}}+\frac{(B_{14}Z_l+B_{34}D_l)^2}{2|\mathbf{M}|B_{44}}\right\}\left\{\cos\theta_i\frac{B_{52}S_l}{B_{55}}\right.$$
$$\left.+\sin\theta\frac{(B_{14}Z_l+B_{34}D_l)}{B_{44}}+\sin\theta\frac{B_{64}d}{B_{44}\mu}\right\}dZ_l dS_l dD_l \quad (20)$$

$$\delta f^2_{pp(Vx+tilt+shadow+Cur)}$$
$$=\frac{8\pi|\mathbf{M}|}{\lambda^2\sigma_{pp}\sqrt{B_{44}B_{55}}}\sqrt{\frac{\pi}{\mu}}\iint\int\sigma^0_{pp}(\theta'_i)\,\Psi\cdot C_{pp}\cdot Sh$$
$$\cdot\exp\left\{\frac{(B_{52}S_l)^2}{2|\mathbf{M}|B_{55}}+\frac{(B_{14}Z_l+B_{34}D_l)^2}{2|\mathbf{M}|B_{44}}+\frac{d^2}{\mu}\right\}$$
$$\cdot\exp\left(\frac{d^2}{\mu}\right)\left\{\alpha+\beta'\frac{d}{\mu}+\chi\frac{1}{2\mu}\left(1+2\frac{d^2}{\mu}\right)\right\}dZ_l dS_l dD_l-\left[f'_{Dpp}\right]^2 \quad (21)$$

with $\beta'\sin^2\theta_i\frac{2(B_{14}Z_l+B_{34}D_l)B_{64}}{B_{44}^2}+2\cos\theta_i\sin\theta_i\frac{B_{52}B_{64}}{B_{55}B_{44}}S_l$.

If the effects of the HM and the horizontal component of orbital

velocity are both ignored, (18) and (19) are further simplified as

$$\begin{aligned} & f'_{Dpp(tilt+shadow+Cur)} \\ &= -\frac{4\pi\,|\mathbf{M}|}{\lambda\sigma_{pp}\sqrt{B_{44}B_{55}}}\sqrt{\frac{\pi}{\mu}}\iiint \sigma^0_{pp}(\theta'_i)\frac{B_{52}S_l}{B_{55}}\,\Psi\cdot C_{pp}\cdot Sh \\ &\quad\cdot\exp\left\{\frac{d^2}{\mu}+\frac{(B_{52}S_l)^2}{2\,|\mathbf{M}|\,B_{55}}+\frac{(B_{14}Z_l+B_{34}D_l)^2}{2\,|\mathbf{M}|\,B_{44}}\right\}\cos\theta_i dZ_l dS_l dD_l \quad (22) \\ & \delta f^2_{pp(tilt+shadow+Cur)} \\ &= \frac{8\pi\,|\mathbf{M}|}{\lambda^2\sigma_{pp}\sqrt{B_{44}B_{55}}}\sqrt{\frac{\pi}{\mu}}\iiint \sigma^0_{pp}(\theta'_i)\cdot\alpha\cdot\Psi C_{pp}\cdot Sh\cdot\exp\left(\frac{d^2}{\mu}\right) \\ &\quad\cdot\exp\left\{\frac{(B_{52}S_l)^2}{2|\mathbf{M}|B_{55}}+\frac{(B_{14}Z_l+B_{34}D_l)^2}{2\,|\mathbf{M}|\,B_{44}}+\frac{d^2}{\mu}\right\}dZ_l dS_l dD_l-\left[f'_{Dpp}\right]^2 \quad (23) \end{aligned}$$

Considering the effect of Bragg frequency, the total Doppler shift f_{Dpp} is obtained as

$$f_{Dpp} = f'_{Dpp(H_y+Vx+tilt+shadow+Cur)} + f_{\text{Bragg}} \quad (24)$$

with

$$f_{\text{Bragg}} = \frac{1}{2\pi}\sqrt{gK_{\text{Bragg}}(\theta_i)} \quad (25)$$

5. NUMERICAL RESULTS AND DISCUSSIONS

In Figs. 1(a) and (b), the predicted Doppler shifts from linear surfaces, in which the HM is not considered, are compared with the numerical simulations performed by Toporkov et al. [9] at L-band (1.3 GHz) radar frequency. The figures show that when we neglect the effect of the TM (we set the local incidence angle $\theta'_i = \theta_i$), the predicted Doppler shifts by (22) are in complete agreement with the free Bragg frequencies. However, if the effect of TM is considered, it is obvious that the predicted Doppler frequencies for HH- and VV-polarization are remarkably larger than the free Bragg frequency. Meanwhile, the predicted Doppler shifts are always found larger in HH polarization than in VV, but eventually come together at very low grazing angles, with their values both recovering the free Bragg frequency. Those interesting phenomena mentioned above can be explained by the following reasons: (1) Doppler shift corresponds to a NRCS-weighted mean line-of-sight velocity of the small scattering facets. Just as shown in Fig. 2, the normalized changing rates of NRCS with large scale waves' slope S_l are obviously larger than zero. Thus, for the case

of upwind configuration, at the regions where the slopes of the so-called long tilting waves are positive, Doppler shifts of scattered fields from small surface elementary scatterers include additional Doppler frequencies due to orbit motions; (2) From Fig. 2, we also can find that the radar signals are more sensitive to S_l in HH polarization than in VV. Therefore, the predicted Doppler shifts in HH polarization are always larger than those in VV; (3) As shown in Fig. 3, at LGA only some scattering facets in the vicinity of the crests can be illuminated. On the other hand, because the horizontal component of orbital velocity has been neglected in (22), the orbit velocities of the scattering facts near crests equal to zero. Thus, the Doppler frequencies for different polarizations predicted by (22) would eventually come together at LGA, with their values being close to recover the free Bragg frequency. Figs. 1(a) and (b) also show that at LGA the Doppler shifts simulated by (20) are separated with the results evaluated by (22) and increase rapidly with incidence angles. The reason for this phenomenon is that in (20) the effect of the horizontal component of the orbit velocity has been considered and at LGA only some scattering facets in the vicinity of the crests, where the horizontal component of the

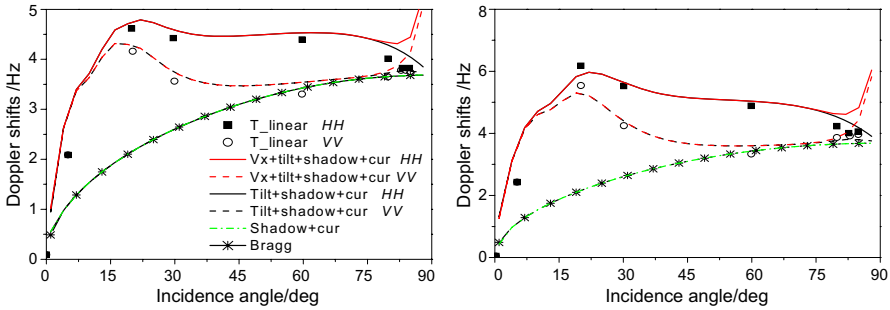

Figure 1. Comparisons of the predicted Doppler shifts when the HM is not taken into account. (a) Windspeed $U_{19.5} = 5\,\mathrm{m/s}$. (b) Windspeed $U_{19.5} = 7\,\mathrm{m/s}$. **T-linear**: Toporkov and Brown results from linear sea surface obtained with the exact numerical method of Ordered Multiple Interactions (MOMI). **Vx + tilt + shadow + cur**: $f'_{Dpp(Vx+tilt+shadow+cur)} + f_{\mathrm{Bragg}}$. **Tilt + shadow + cur**: $f'_{Dpp(tilt+shadow+cur)} + f_{\mathrm{Bragg}}$. **Shadow + cur**: $f'_{Dpp(shadow+cur)} + f_{\mathrm{Bragg}}$, where $f'_{Dpp(shadow+cur)}$ is simulated (22) when the local incidence angle in the integral has been set to be $\theta'_i = \theta_i$. **Bragg**: The free Bragg frequency f_{Bragg}.

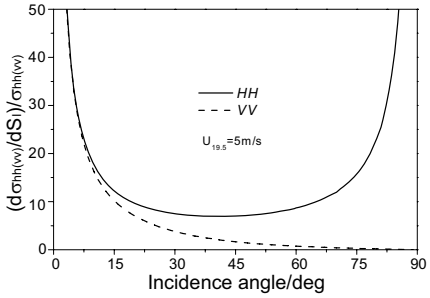

Figure 2. The normalized changing rates of NRCS with large scale waves' slope for HH and VV polarizations.

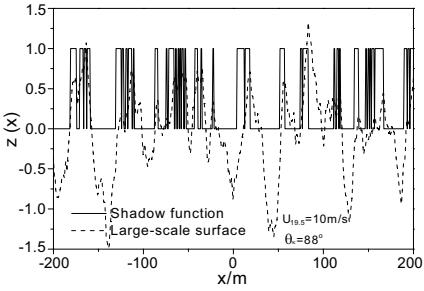

Figure 3. The shadow of the large-scale wave.

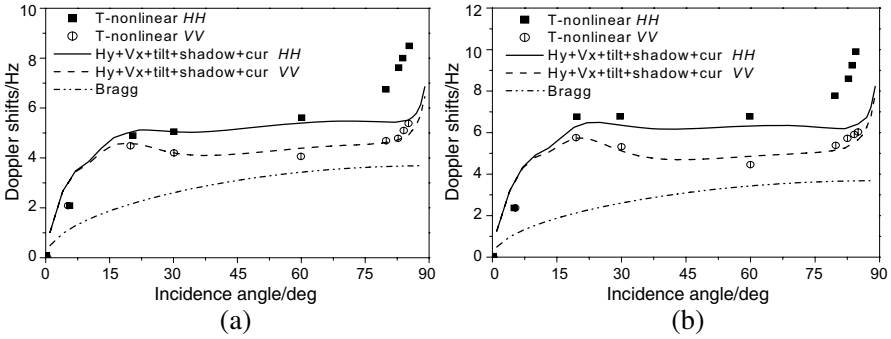

Figure 4. Comparisons of the predicted Doppler shifts when the HM is taken into account. (a) Windspeed $U_{19.5} = 5\,\mathrm{m/s}$. (b) Windspeed $U_{19.5} = 7\,\mathrm{m/s}$. **T-nonlinear**: Toporkov and Brown results from nonlinear Creamer sea surface obtained by MOMI. **Hy + Vx+tilt + shadow + cur**: $f'_{Dpp(Hy+Vx+tilt+shadow+cur)} + f_{\mathrm{Bragg}}$. **Bragg**: The free Bragg frequency f_{Bragg}.

orbit velocity is larger, should be illuminated because of the shadow effect.

Figures 4(a) and (b) show the evolution of Doppler shift with incidence angle. Here, the additional Doppler shift $f'_{Dpp(H_y+Vx+tilt+shadow+cur)}$ is evaluated by Equation (18), in which the HM has been considered. For comparisons, Toporkov and Brown results (T-$nonlinear$) obtained with MOMI and the Creamer sea surface model, which is frequently used to describe weakly nonlinear sea surfaces, are also shown. From the comparisons between the curves in Fig. 4 and in Fig. 1, we

can find that the HM is liable to increase Doppler shift for both polarizations. From Fig. 4, we also can find that the Doppler shifted predicted by (18) can fit Toporkov's results well in VV polarization. However, noticeable differences in HH polarization remain at LGA due to unknown reason.

Figures 5(a) and (b) show the bandwidths δf_{pp} obtained by (19) and (23) at L-band (1.3 GHz) radar frequency. As shown in Figs. 5(a) and (b), the bandwidths are insensitive to radar polarization. From Fig. 5, one also can find that the bandwidths predicted by (19), in which the horizontal component of orbital velocity has been considered, fit the results simulated by Toporkov and Brown with nonlinear Creamer sea surfaces well. On the other hand, the bandwidths predicted by (23), in which the horizontal component of orbital velocity has been neglected, are in good agreement with Toporkov and Brown's results from linear sea surfaces. The horizontal component of large-scale waves' orbital velocity induces an obvious effect on bandwidth. And the results predicted by (19) are found much larger than those predicted by (23) and quasi-insensitive to the incidence angles from 40° to 80°, while the counterparts predicted by (23) fall off rapidly. At very low-grazing angles, the bandwidths predicted by (19) would also become somewhat narrower due to the shadow effect of large-scale waves. Comparisons between the curves shown in Fig. 5(a) and Fig. 5(b) show that the predicted bandwidths are increasing with wind speed.

Figures 6(a) and (b) illustrate the influences of the tilt, the shadow, and the curvature of large-scale waves on Doppler shift and bandwidth more clearly at LGA. In Fig. 6, the radar frequency and the wind speed are the same as those in Fig. 5(a). As shown in the figures,

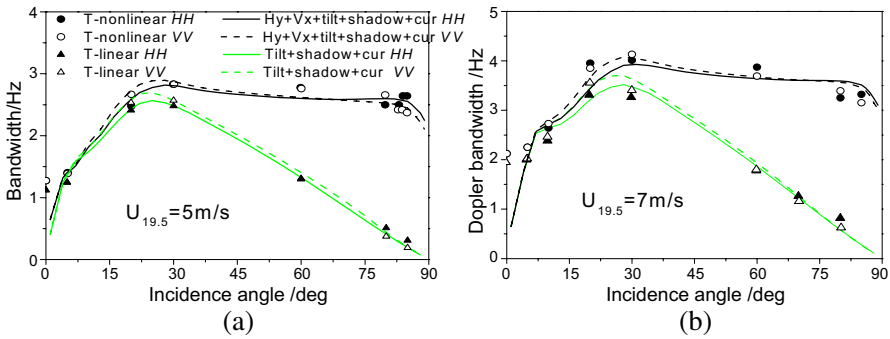

Figure 5. Comparisons of predicted bandwidths in L-band at different windspeeds. (a) $U_{19.5} = 5\,\mathrm{m/s}$. (b) $U_{19.5} = 7\,\mathrm{m/s}$.

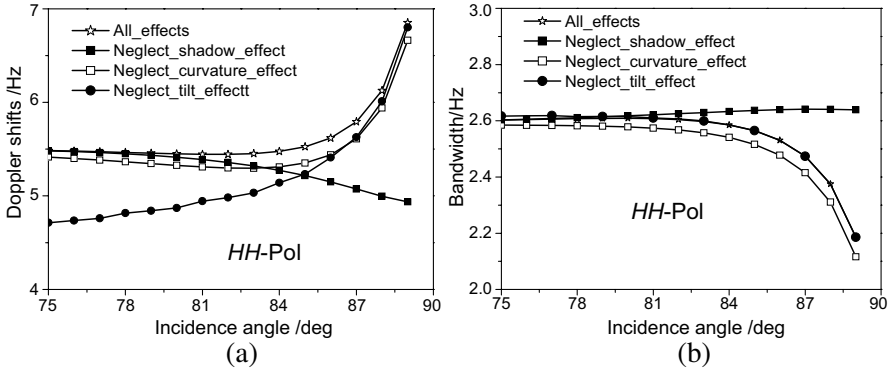

Figure 6. The effects of different factors on Doppler shift and bandwidth. (a) Doppler shift. (b) Bandwidth.

long waves' shadow induces an increase in Doppler shift and a decrease in bandwidth. If we neglect the effect of long waves' curvature, the values of the predicted Doppler shift and the bandwidth will become somewhat smaller. On the other hand, one can also find that long waves' tilt lead to a remarkable effect on Doppler shift. However, as shown in Fig. 6(a), this tilt effect on Doppler shift will become smaller with incident angle at LGA. From Fig. 6(b) one can find that the predicted bandwidth is almost not changed by long waves tilt. For VV-polarization signals, similar conclusions can be obtained.

6. CONCLUSION

In this paper, we have investigated the characteristics of the microwave Doppler spectra of sea echoes and derived the analytical formulas for Doppler shift and bandwidth within the framework of the composite surface scattering model. Comparisons have been made with the exact numerical simulations performed by Toporkov and Brown and with Doppler measurements. From the results, we can find that the values of Doppler shifts for HH- and VV-polarization are elevated by the TM and the HM. Because the scattering cross section in HH-polarization is more sensitive to large scale waves' slope, the central Doppler shift for HH-polarization is always larger than that in VV-polarization. At moderate-incidence angles, the shadow effect as well as the horizontal-component of the large-waves orbit velocity will not induce any impact on Doppler shifts. However, at LGA, the shadow and the horizontal-component of large-waves orbit velocity result in a rapid increase in Doppler shifts. On the other hand, if the horizontal

component of orbital velocity has been considered, the bandwidths are quasi-insensitive to the incidence angles at moderate-incidence angles. However, at LGA, shadow effect makes the bandwidths become somewhat narrower. If we do not take the effect of the horizontal component of orbital velocity into account, the bandwidths will fall off rapidly at moderate- and low-grazing angles. From the results, we also find that the spectral widths are insensitive to radar polarization.

ACKNOWLEDGMENT

This research was supported by the Young Scientists Fund of the National Natural Science Foundation of China (Grant No. 40906088, 41106153) and the National Science Foundation for Distinguished Young Scholars of China (Grant No. 61225002).

REFERENCES

1. Crombie, D. D., "Doppler spectrum of sea echo at 13.66 Mc./s.," *Nature*, Vol. 175, 681–682, 1955.
2. Bass, F. G., I. M. Fuks, A. I. Kalmykov, I. E. Ostrovsky, and A. D. Rosenberg, "Very-high frequency radiowave scattering by a disturbed sea surface. Part II: Scattering from an actual sea surface," *IEEE Trans. Antennas Propagat.,* Vol. 16, 560–568, 1968.
3. Wright, J. W. and W. C. Keller, "Doppler spectra in microwave scattering from wind waves," *Phys. Fluids*, Vol. 14, 466–474, 1971.
4. Zavorotny, V. U. and A. G. Voronovich, "Two-scale model and ocean radar Doppler spectra at moderate- and low-grazing angles," *IEEE Trans. Antennas Propagat.*, Vol. 46, 84–92, 1998.
5. Nie, D., M. Zhang, X.-P. Geng, and P. Zhou, "Investigation on Doppler spectral characteristics backscattered echoes from nonlinear surface of finite-depth sea," *Progress In Electromagnetics Research*, Vol. 130, 169–186, 2012.
6. Qi, C., Z. Zhao, W. Yang, Z. Nie, and G. Chen, "Electromagnetic scattering and Doppler analysis of three-dimensional breaking wave crests at low-grazing angles," *Progress In Electromagnetics Research*, Vol. 119, 239–252, 2011.
7. Soriano, G., M. Joelson, M. Saillard, and P. C. Marseille, "Doppler spectra from a two-dimensional ocean surface at L-band," *IEEE Trans. Geosci. Remote Sensing*, Vol. 44, 2430–2437, 2006.
8. Fuks, I. M. and A. G. Voronovich, "Radar backscattering from

Gerstner's sea surface," *Waves in Random Media*, Vol. 12, 321–339, 2002.

9. Toporkov, J. V. and G. S. Brown, "Numerical simulations of scattering from time-varying randomly rough surfaces," *IEEE Trans. Geosci. Remote Sensing,* Vol. 38, 1616–1625, 2000.
10. Johnson, J. T., J. V. Toporkov, and G. S. Brown, "A numerical study of back-scattering from time-evolving sea surfaces: Comparison of hydrodynamic models," *IEEE Trans. Geosci. Remote Sensing*, Vol. 39, 2411–2420, 2001.
11. Hayslip, A. R., J. T. Johnson, and G. R. Baker, "Further numerical studies of back-scattering from time-evolving nonlinear sea surfaces," *IEEE Trans. Geosci. Remote Sensing*, Vol. 41, 2287–2293, 2003.
12. Saillard, M., P. Forget, G. Soriano, M. Joelson, P. Broche, and P. Currier, "Sea surface probing with L-band Doppler radar: Experiment and theory," *C. R. Physique*, Vol. 6, 675–682, 2005.
13. Hisaki, Y., "Doppler spectrum of radio wave scattering from ocean-like moving surfaces for finite illuminated area," *Int. J. Remote Sensing*, Vol. 24, 3075–3091, 2003.
14. Nouguier, F., C. A. Guerin, and G. Soriano, "Analytical techniques for the Doppler signature of sea surfaces in the microwave regime — I: Linear surfaces," *IEEE Trans. Geosci. Remote Sensing*, Vol. 49, No. 12, 4856–4864, 2011.
15. Nouguier, F., C. A. Guerin, and G. Soriano, "Analytical techniques for the Doppler signature of sea surfaces in the microwave regime — II: Nonlinear surfaces," *IEEE Trans. Geosci. Remote Sensing*, Vol. 49, No. 12, 4920–4927, 2011.
16. Wang, Y. H. and Y. M. Zhang, "Investigation on Doppler shift and bandwidth of backscattered echoes from a composite sea surface," *IEEE Trans. Geosci. Remote Sensing,* Vol. 49, 2287–2293, 2011.
17. Wang, Y. H., Y. M. Zhang, M. X. He, and C. F. Zhao, "Doppler spectra of microwave scattering fields from nonlinear oceanic surface at moderate- and low-grazing angles," *IEEE Trans. Geosci. Remote Sensing,* Vol. 50, No. 4, 1104–1116, 2012.
18. Pidgeon, V. W., "Doppler dependence of radar sea return," *J. Geophys. Res.*, Vol. 73, 1333–1341, 1968.
19. Valenzuela, G. R. and M. B. Laing, "Study of Doppler spectra of radar sea echo," *J. Geophys. Res.*, Vol. 75, 551–563, 1970.
20. Plant, W. J., "A model for microwave Doppler sea return at high incidence angles: Bragg scattering from bound, tilted waves," *J.*

Geophys. Res., Vol. 102, 21131–21146, 1997.

21. Lamont-Smith, T., "Doppler spectra of laboratory wind waves at low grazing angle," *Waves in Random Media*, Vol. 10, 33–41, 2000.
22. Romeiser, R. and D. R. Thompson, "Numerical study on the along-track interferometric radar imaging mechanism of oceanic surface currents," *IEEE Trans. Geosci. Remote Sensing*, Vol. 38, 446–458, 2000.
23. Alpers, W. and K. Hasselmann, "The two-frequency microwave technique for measuring ocean-wave spectra from an airplane or satellite," *Boundary Layer Meteorol*, Vol. 13, 215–230, 1978.
24. Alpers, W., D. B. Ross, and C. L. Rufenach, "On the detectability of ocean surface waves by real and synthetic aperture radar," *J. Geophys. Res.*, Vol. 86, 6481–6498, 1981.
25. Fisz, M., *Probability Theory and Mathematical Statistics*, Krieger Pub. Co., 1980.
26. Keller, W. C. and W. J. Plant, "Microwave backscatter from the sea: Modulation of received power and Doppler bandwidth by long waves," *J. Geophys. Res.*, Vol. 99, 9751–9766, 1994.
27. Ulaby, F. T., R. K. Moore, and A. K. Fung, *Microwave Remote Sensing,* Vol. 2, Addison-Wesbey, Reading, MA, 1982.
28. Voronovich, A. G. and V. U. Zavorotny, "Curvature effects in the composite model for low-grazing-angle rough-surface scatter," *Waves in Random Media*, Vol. 8, 41–52, 1998.
29. Smith, B. G., "Lunar surface roughness: Shadowing and thermal emission," *J. Geophys. Res.*, Vol. 72, 4059–4067, 1967.